




Kaleidoscope of phases tuned by global dipole orientations in the Hubbard modelTiago Mendes-Santos ^{1,2,*}, Rubem Mondaini ^{3,†}, Thereza Paiva,² and Raimundo R. dos Santos ²¹*Theoretical Physics III, Center for Electronic Correlations and Magnetism, Institute of Physics, University of Augsburg, 86135 Augsburg, Germany*²*Instituto de Física, Universidade Federal do Rio de Janeiro Cx.P. 68.528, 21941-972 Rio de Janeiro RJ, Brazil*³*Beijing Computational Science Research Center, Beijing 100193, China*

(Received 21 August 2023; accepted 27 October 2023; published 14 November 2023)

We investigate the emergence of a myriad of phases in the strong coupling regime of the dipolar Hubbard model in two dimensions. By using a combination of numerically unbiased methods in finite systems with analytical perturbative arguments, we show the versatility that trapped dipolar atoms possess in displaying a wide variety of many-body phases, which can be tuned by changing the collective orientation of the atomic dipoles. We further investigate the stability of these phases to thermal fluctuations in the strong coupling regime, highlighting that they can be accessed with current techniques employed in cold atoms experiments on optical lattices. Interestingly, both quantum and thermal phase transitions are signaled by the behavior of density-density and local moment-local moment correlations, which are available through quantum gas microscopy for cold atoms to be used as probes for the onset of different phases.

DOI: [10.1103/PhysRevB.108.205128](https://doi.org/10.1103/PhysRevB.108.205128)**I. INTRODUCTION**

Experiments with ultracold atoms on optical lattices [1–4] have stimulated the search for new paradigms in many-body physics, especially due to the possibility of controlling and engineering quantum macroscopic states [5]. A recent experimental advance is the manipulation of atoms or molecules with (electric or magnetic) dipoles [6–12]. For example, ⁵²Cr atoms with a large magnetic moment ($6\mu_B$, with μ_B being the Bohr magneton) form Bose-Einstein condensates (BEC's) below $T_c \simeq 700$ nK [13]; larger magnetic moments, $\sim 12\mu_B$, were later obtained with Er₂ molecules [14]. The first quantum degenerate dipolar Fermi gas was realized [15] with ¹⁶¹Dy atoms cooled down to 20% of the Fermi temperature, $T_F \approx 300$ nK; also, Fermi surface deformation was observed in Er atoms [16]. An ultracold dense gas of fermionic potassium-rubidium (⁴⁰K-⁸⁷Rb) polar molecules was also generated [17], which paved the way to trap them into 2D and 3D optical lattices [18]; and two-component Er dipolar fermionic gas with tunable interactions was prepared with collisional stability in the strongly interacting regime [10].

The interest in dipolar atoms stems from their long-ranged and anisotropic interactions, such that they can be directionally repulsive or attractive. This adds extra richness to the diversity of collective states of atoms in an optical lattice [19,20]. For instance, quantum magnetism of high-spin systems has been experimentally studied with bosonic [21,22] and fermionic [23] atoms, as well as with molecules [24] in optical lattices, and the ability to design quantum spin Hamiltonians with cold atoms may lead to the development

of error-resilient qubit encoding and to topologically protected quantum memories [25]. In addition, since one of the motivations to study cold atoms in optical lattices is the possibility of emulating condensed matter models [1–4], a detailed investigation of effects due to dipolar interactions is clearly of interest.

The study of dipolar physics with trapped atoms and molecules has experienced an increased interest in recent years [11,26]. Indeed, several studies suggest that new phenomena may emerge, such as *p*-wave pairing [27,28] and different density-wave patterns [29–38], some of which are analyzed through analogies with liquid-crystals. The increased stability in recent experiments allowed for observing super-solid behavior in dipolar quantum gases [39–41]. Another remarkable experiment progress comes from imaging, as site-resolved correlations were measured for molecules [24] and dipolar bosons [12].

The extended Hubbard Model was realized in different platforms, such as semiconductor dipolar excitons confined in a GaAs quantum well [42], with spin valley isospins arising in chiral-stacked twisted double bilayer graphene [43], and on semiconductor quantum dots [44,45]. Due to the long-range nature of dipolar interactions, the extended Hubbard Model emulated by dipolar fermionic [10] and bosonic [12,46] atoms on optical lattices differ from the previous ones, not only because interactions go beyond near-neighbor sites, but also because of its dependence on the dipole direction, opening up the possibility for new phases to emerge.

Considering the aforementioned rich variety of phenomena, here we present a study of the dipolar Hubbard model in two dimensions. The layout of the paper is as follows. In Sec. II, we discuss the model and methodology used to extract its physical properties. In Sec. III, we discuss ground-state properties for different polarization directions, extracted from

*tmsantos.if@gmail.com

†rmondaini@csr.ac.cn

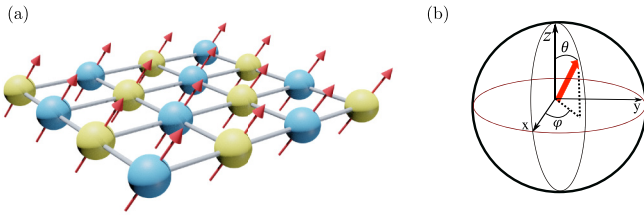


FIG. 1. (a) Schematic representation of the lattice populated by the magnetic dipoles, which possess global coinciding orientation. The two different site colors represent the two hyperfine states, and the phase depicted is the Mott phase (see text). (b) Definition of the polar angles describing the direction of the magnetic dipoles, shown as a thick (red) arrow.

Lanczos diagonalizations; finite-size effects are also probed, aided by analyses both in the atomic limit (i.e., $t = 0$) and through perturbation theory. Some thermal effects are discussed in Sec. IV. Last, Sec. V summarizes our findings.

II. MODEL AND METHODS

We consider *spinful* atoms (i.e., a mixture of atoms in two hyperfine states) on an optical lattice. The system is described by the Hamiltonian,

$$\hat{\mathcal{H}} = -t \sum_{\langle \mathbf{i}, \mathbf{j} \rangle, \sigma} (\hat{c}_{\mathbf{i}\sigma}^\dagger \hat{c}_{\mathbf{j}\sigma} + \text{H.c.}) + U \sum_{\mathbf{i}} \hat{n}_{\mathbf{i}\uparrow} \hat{n}_{\mathbf{i}\downarrow} + \sum_{\mathbf{i} \neq \mathbf{j}} V_{\mathbf{ij}} \hat{n}_{\mathbf{i}} \hat{n}_{\mathbf{j}}, \quad (1)$$

where $\hat{c}_{\mathbf{i}\sigma}$ ($\hat{c}_{\mathbf{i}\sigma}^\dagger$) denotes the particle annihilation (creation) operator and $\hat{n}_{\mathbf{i}}$ the number operator at site \mathbf{i} . The sums run over sites of a square optical lattice, with $\langle \mathbf{i}, \mathbf{j} \rangle$ denoting nearest neighbor sites; $\sigma = \uparrow, \downarrow$ denotes the two hyperfine states, and t is the hopping integral. An external field aligns the dipoles parallel to the unit vector $\hat{\mathbf{d}}$, specified by the usual polar angles θ and φ , taking $\hat{\mathbf{z}}$ perpendicular to the square lattice; see Fig. 1(b). The dipolar interaction is then written as

$$V_{\mathbf{ij}} = \frac{V}{r_{\mathbf{ij}}^3} [1 - 3(\hat{\mathbf{r}} \cdot \hat{\mathbf{d}})^2], \quad (2)$$

where V (proportional to the square of the dipole moments) is the strength of the interaction, $\mathbf{r}_{\mathbf{ij}} \equiv \mathbf{i} - \mathbf{j}$ is a vector joining sites on the lattice, and $\hat{\mathbf{r}}$ is its unit vector. The interaction of two atoms in the same optical well, U , is the sum of two contributions: one is the usual onsite repulsive interaction, tunable through a Feshbach resonance; the other comes from the dipolar interaction, whose behavior at small distances is limited by the finite size of the atoms [6,47].

The ground-state properties of the Hamiltonian [Eq. (1)] are analyzed with the Lanczos method [48–50] on a 4×4 lattice with periodic boundary conditions, in the subspace of half filling; translational symmetry and total spin projection are also incorporated in the bases used. In line with experiments in the absence of dipolar interactions, here we consider the case $U = 8t$, which is also convenient since finite-size effects are small in the strong-coupling regime – more on this below. The finite lattice size we use forces us to truncate the dipolar interaction beyond second neighbors. Nonetheless, anisotropy and competition between attractive and repulsive

couplings are preserved. We also perform strong-coupling analyses [51,52], complemented by simulated annealing [53], to check the consistency of exact diagonalization results and to consider the effects of thermal fluctuations; details will be presented in Secs. III, IV, and in the Appendix.

Here we borrow the attribute *spin* familiar from the condensed matter context, to denote *atomic species*.

Accordingly, we define:

- (i) spin-spin correlation functions,

$$C_s(\mathbf{r}) \equiv \langle \hat{m}_0 \hat{m}_{\mathbf{r}} \rangle, \quad \hat{m}_{\mathbf{r}} = \hat{n}_{\mathbf{r}\uparrow} - \hat{n}_{\mathbf{r}\downarrow}, \quad (3)$$

- (ii) connected density-density correlation functions,

$$C_d(\mathbf{r}) \equiv \langle \hat{n}_0 \hat{n}_{\mathbf{r}} \rangle - \langle \hat{n}_0 \rangle \langle \hat{n}_{\mathbf{r}} \rangle, \quad \hat{n}_{\mathbf{r}} = \hat{n}_{\mathbf{r}\uparrow} + \hat{n}_{\mathbf{r}\downarrow}, \quad (4)$$

- (iii) connected local moment-local moment (from now on referred to as moment-moment) correlation functions,

$$C_m(\mathbf{r}) \equiv \langle \hat{m}_0^2 \hat{m}_{\mathbf{r}}^2 \rangle - \langle \hat{m}_0^2 \rangle \langle \hat{m}_{\mathbf{r}}^2 \rangle; \quad (5)$$

this latter quantity is most readily accessible in experiments [54–57], and, as we will see, carries the signature of both quantum and thermal phase transitions. Density-density correlation functions are also available in quantum gas microscopy and were used to characterize the different phases in recent experiments with dipolar bosonic Erbium atoms [12].

III. ZERO-TEMPERATURE PHASE DIAGRAM

In this section we discuss the zero-temperature phase transitions induced by the variation of both the polarization, θ and φ , and the strength of the dipolar interaction, V ; we will also compare results for $U = 0$ and in the strong coupling regime.

A. Phase diagram— $\varphi = 0$

Let us first fix the direction of polarization and vary the strength of the dipolar interaction, V . Figures 2(a) show the correlation functions for the isotropic case, $\theta = \varphi = 0$: spin correlations consistent with a Néel-like arrangement (a1) are completely suppressed at $V_{\text{CB}} \approx 3.1$, beyond which density correlations (a2) develop. The system therefore goes from a Mott phase, in which each species occupies one sublattice, to a checkerboard charge density wave (cbCDW) phase, in which only one of the sublattices is occupied by both species; see cartoons in Fig. 2(d). It is interesting to compare this with the usual extended Hubbard model (EHM), in which case the interaction is cut off at the nearest-neighbor site [58–62], such that $V_c^{\text{EHM}} = U/4$ in the atomic limit, separating the Mott and CDW phases. In the presence of diagonal interactions of strength V_d , the cbCDW phase is stabilized for $V_{\text{CB}} > V_c^{\text{EHM}} + 3V_d$; that is, additional repulsion along the diagonals favors the Mott phase. Panel (a3) shows the moment-moment correlation function, which captures the increase of fluctuations at the critical point. The sharp drop in the local moment is responsible for the sharpness of $C_m(\mathbf{r})$ at the transition; see below. By contrast, when the dipoles point along the $\hat{\mathbf{x}}$ direction [Figs. 2(b)] the transition is from a Mott phase to a striped phase, at a smaller V_c than for the isotropic case; the direction of the stripes is that of the dipoles, since arranging them head-to-tail lowers the energy and skipping a row costs less energy than placing them on adjacent rows. As a result,

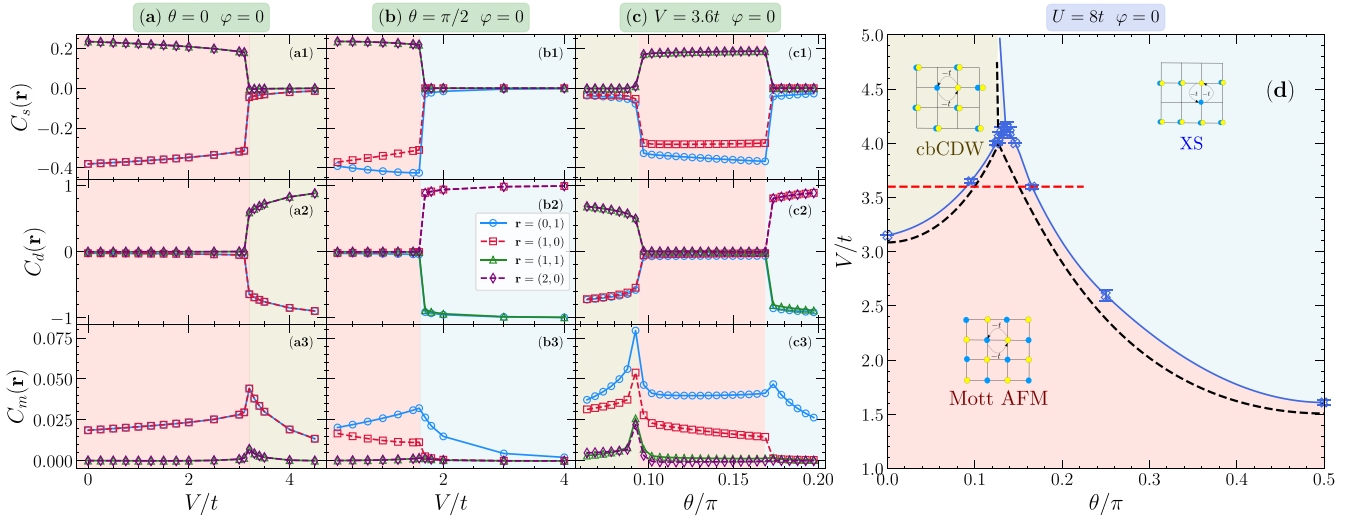


FIG. 2. Panels (a) and (b) show the dependence of the different correlation functions with the dipolar interaction strength, V/t , for dipoles perpendicular (a) and parallel (b) to the lattice; panels (c) show the dependence with the polar angle θ/π , at fixed V/t . Each curve is for a fixed distance, \mathbf{r} , as indicated in panel (b2). These correlation functions are obtained with Lanczos diagonalization on a 4×4 lattice. Panel (d) shows the phase diagram $V/t \times \theta/\pi$ for $U/t = 8$ and $\varphi = 0$: data points are Lanczos diagonalization results (full lines guide the eye) for $t = 1$, while the dashed line corresponds to the atomic limit ($t = 0$).

nearest-neighbor spin correlations are now anisotropic in the Mott phase: in strong coupling, the effective nearest neighbor exchange interaction $J_{v,\text{eff}} = 4t^2/(U - V_v)$, $v = x, y$, possesses $V_x < 0$ and $V_y > 0$, so that attraction weakens magnetic correlations. By the same token, local moment fluctuations are also anisotropic, since vertically one has doublon-holon pairs while horizontally one has doublon-doublon pairs, the latter being less prone to fluctuations than the former.

Since the nature of the CDW state depends on the polarization angle, we now probe the phase transitions driven by changing the direction of the dipoles within the xz plane ($\varphi = 0$), while V is kept fixed. Figures 2(c) show that with increasing θ the cbCDW phase gives way to a Mott phase (with anisotropic correlations), and further increase in θ drives the system to another CDW phase, now with stripes along the \hat{x} direction (XS); see the horizontal dashed line in Fig. 2(d). This intervening Mott phase disappears at some critical V_c , which is not very sensitive to the hopping presence for a fixed U/V in the physically relevant domain of $U \gg t$. This is revealed by comparing with the size-independent strong coupling results for the cbCDW, Mott, and striped phases listed in the Appendix; see black-dashed lines in Fig. 2(d). Note that for $V < V_{\text{CB}} \approx 3.1t$ no cbCDW state is formed, and the smaller V gets, the closer to the plane the direction of polarization must get to reach the XS phase; interestingly, below $V_H \approx 1.5t$ no CDW is formed.

B. Phase diagram— $\theta \times \varphi$

To relax the constraint of polarization within the xz plane, we may take advantage of the fact that the atomic limit (i.e., $t \rightarrow 0$) captures, to a very good approximation, the essence of the phase diagrams [as discussed in connection with Fig. 2(d)] and in what follows we start by describing the $t = 0$ limit. We then discuss how quantum fluctuations ($t \neq 0$) affect the

$\theta \times \varphi$ phase diagram by employing second-order perturbation theory and considering the behavior of the different correlation functions.

1. Atomic limit $t = 0$

A systematic search for the ground state in the atomic limit may start by setting $U = 0$ and looking for minima of the Fourier transform of the dipolar potential between two particles,

$$V_{\mathbf{q}} = \frac{1}{L^2} \sum_{\mathbf{i}, \mathbf{j}} e^{i\mathbf{q} \cdot \mathbf{r}_{ij}} V_{ij}, \quad (6)$$

where L is the linear lattice size, and $q_\alpha = 2n_\alpha\pi/L$, with $\alpha = x, y$, and $n_\alpha = 0, \dots, L$; we set the lattice spacing to unity. Figure 3 shows $V_{\mathbf{q}}$ for several dipole orientations (θ, φ). For $(\theta, \varphi) = (0, 0)$, $V_{\mathbf{q}}$ is minimized for $\mathbf{q}_{\text{min}} = (\pi, \pi)$, which corresponds to a cbCDW state also at $U = 0$, as expected from the analyses of Sec. III A.

For dipoles in the plane, $\theta = \pi/2$, if $\varphi = 0$ the minima are at $\mathbf{q}_{\text{min}} = (0, \pi)$, thus giving rise to \hat{x} -oriented stripes; see the inset of Fig. 2(d). Similarly, if $\varphi = \pi/2$ instead, the minima are at $\mathbf{q}_{\text{min}} = (\pi, 0)$, thus giving rise to \hat{y} -oriented stripes. For dipoles still in the plane, but oriented along a lattice diagonal, $\varphi = \pi/4$, there is a degeneracy larger than before: the minima are located at $\mathbf{q}_{\text{min}} = (\delta, 2\pi - \delta)$ [or, equivalently, to $\mathbf{q}_{\text{min}} = (2\pi - \delta, \delta)$], with $\delta \sim 2\pi/L$, in addition to $\mathbf{q}_{\text{min}} = (0, 0)$; as we will see below, these correspond to phase-separated distributions. Finally, Fig. 3(e) corresponds to dipoles at an angle of $\pi/4$ above the plane and with projections on the plane lying along the lattice diagonals: these lead to $\mathbf{q}_{\text{min}} = (3\pi/2, \pi/2)$ [or, equivalently, to $\mathbf{q}_{\text{min}} = (\pi/2, 3\pi/2)$] which corresponds to a diagonally striped, or tilted CDW phase; see Fig. 16 in the Appendix.

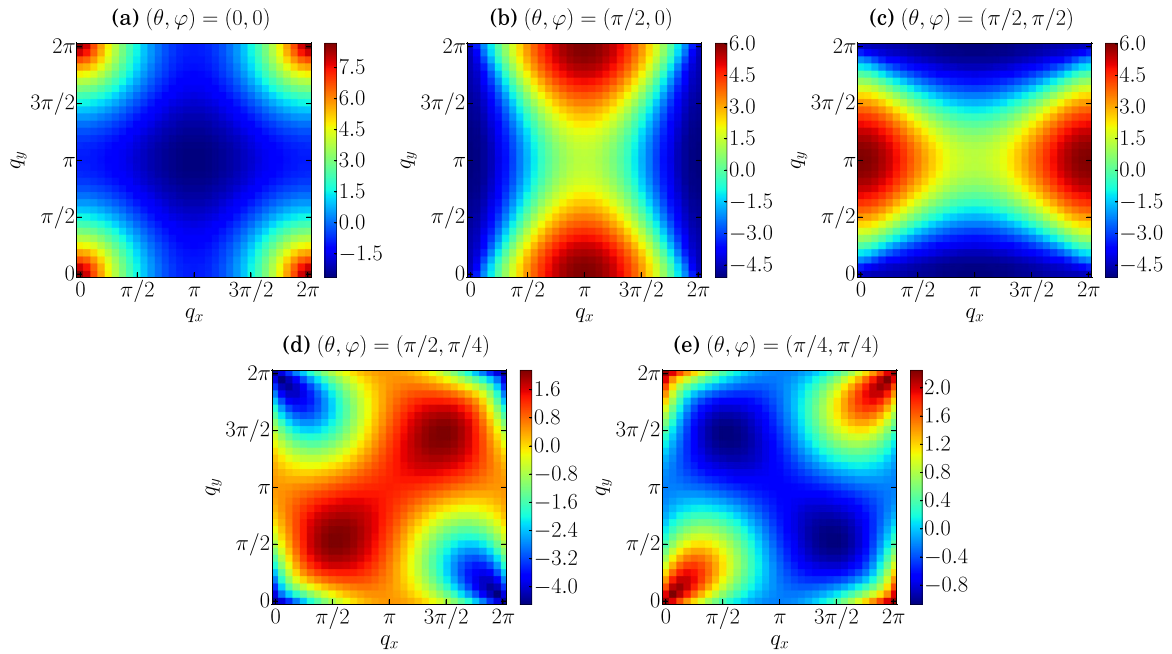


FIG. 3. Fourier transform of the dipolar potential, Eq. (6), for dipoles oriented along the (a) $(0, 0)$, (b) $(\pi/2, 0)$, (c) $(\pi/2, \pi/2)$, (d) $(\pi/2, \pi/4)$, and (e) $(\pi/4, \pi/4)$ directions, and for a 32×32 lattice. The wavevectors are in units of the inverse lattice spacing.

We now discuss how \mathbf{q}_{\min} evolves as one changes θ (or φ) for a fixed φ (or θ). As it can be seen from Fig. 4(a), for $\varphi = 0$, the minima at $\mathbf{q}_{\min} = (\pi, \pi)$ (cbCDW configuration) changes to $\mathbf{q}_{\min} = (0, \pi)$ (X-striped) as the angle θ increases above $\theta \approx 0.15$, in agreement with the results discussed in Sec. III A. Interestingly, for $\theta = \pi/4$, between the Y-striped phase [$\mathbf{q}_{\min} = (\pi, 0)$] and the X-striped phase [$\mathbf{q}_{\min} = (0, \pi)$] the variation of φ induces different wave-vectors \mathbf{q}_{\min} for $0.15 \leq \varphi \leq 0.33$ [see Fig. 4(b)], suggesting that multiple tilted CDW phases are stabilized as ground states.

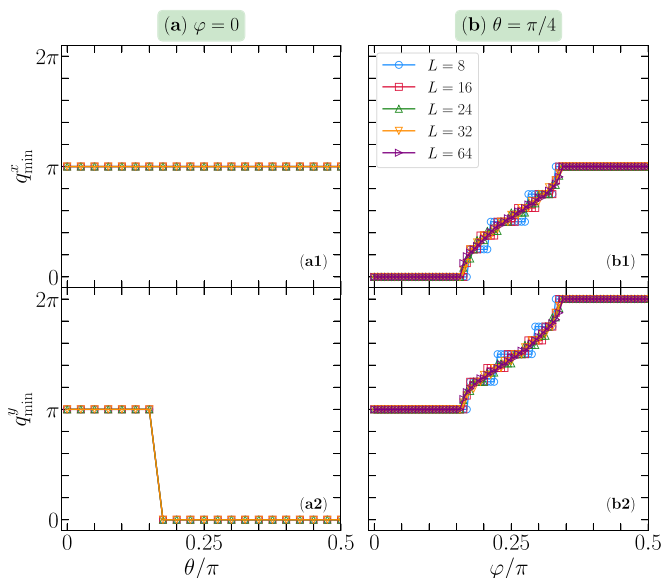


FIG. 4. Wave-vectors $\mathbf{q}_{\min} = (q_{\min}^x, q_{\min}^y)$ as a function of (a) θ for $\varphi = 0$ and (b) φ for $\theta = \pi/4$.

Our next step is to check the stability of these prospective ground states at half-filling with respect to (i) lattice size, (ii) dipolar interaction cutoff range, and (iii) the presence of an onsite interaction, U . We fix $(\theta, \varphi) = (\pi/4, \pi/4)$ and compare three different configurations: Mott insulator, cbCDW, and the tilted-CDW configuration associated with $\mathbf{q}_{\min} = (\pi/2, 3\pi/2)$; see Fig. 16 in the Appendix. Figure 5 shows that for $U/V = 0$ and $U/V = 2.2$, increasing the system size does not change the nature of the ground state. When the cutoff in V is set at the second nearest neighbor, as in Figs. 5(a1) and 5(a2), the energy is independent of system size (for sizes

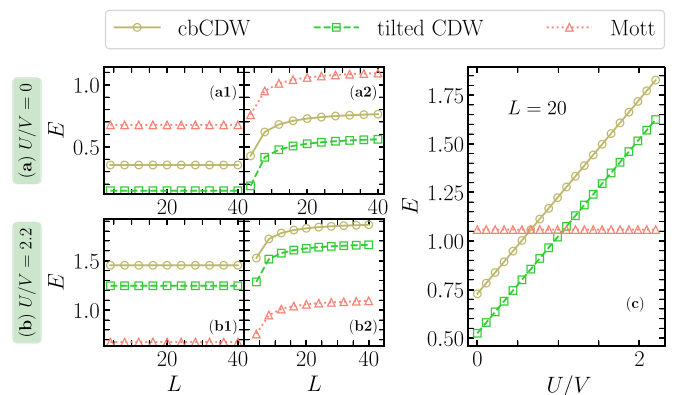


FIG. 5. Size dependence of the energy per number of particles for $(\theta, \varphi) = (\pi/4, \pi/4)$; (a) $U/V = 0$ and (b) $U/V = 2.2$. In panels (a1) and (b1), the dipolar interaction is cut off beyond second neighbors, while in panels (a2) and (b2), the full range compatible with the lattice size is taken into account. The corresponding wave-vectors for the cbCDW and tilted-CDW states are $\mathbf{q} = (\pi, \pi)$ and $\mathbf{q} = (\pi/2, 3\pi/2)$, respectively. Panel (c) shows the dependence of E with U/V for the full-ranged interactions case in a 20×20 lattice.

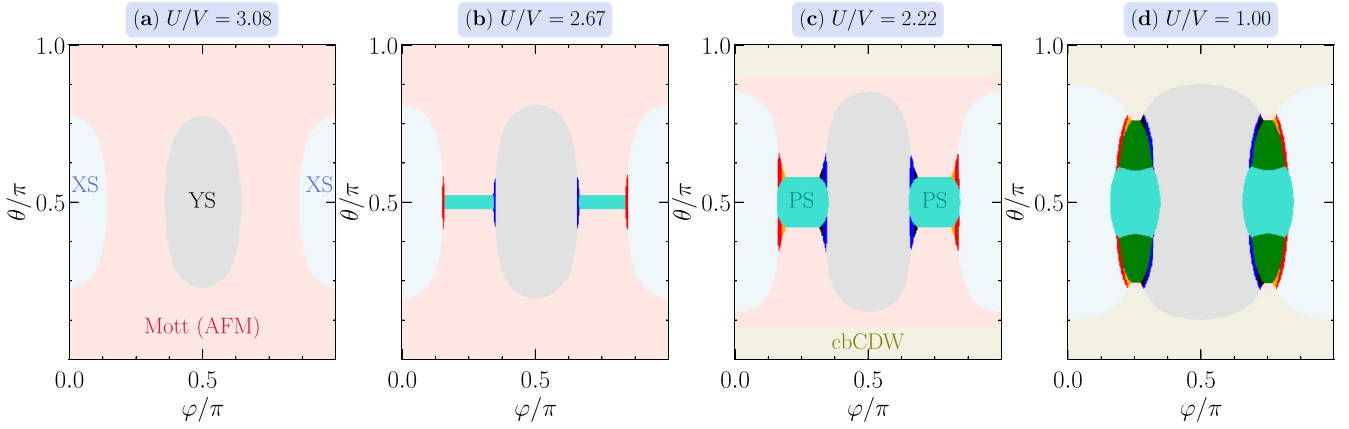


FIG. 6. Ground-state phase diagrams in terms of θ/π and φ/π obtained in the atomic limit for (a) $U/V = 3.08$, (b) $U/V = 2.67$, (c) $U/V = 2.22$, and (d) $U/V = 1.00$. Striped phases along the \hat{x} (XS) and \hat{y} (YS) directions, checkerboard CDW (cbCDW), phase-separated phases (PS), Mott insulating phase, and different diagonally striped phases are present (remaining colors that are not annotated, see Fig. 7).

larger than the cutoff). Allowing for long-range dipolar interactions, with V reaching all sites in the lattice, as displayed in Figs. 5(b1) and 5(b2), the energies clearly converge fast with L , and they are shifted to larger values when compared with the short-ranged V data of Figs. 5(a1) and 5(a2). Figure 5(c) shows that, within the atomic limit approximation, decreasing U/V takes the system from a Mott insulator (for $U/V \geq 1.0$) to a tilted-CDW phase (for $U/V \lesssim 1.0$). For this particular choice of $(\theta, \varphi) = (\pi/4, \pi/4)$, $V_x = V_y$ and the anisotropy comes from longer ranged interactions, therefore larger values of V , i.e., smaller U/V are necessary to tilt the CDW. The presence of a tilted-CDW configuration as the ground state for $(\theta, \varphi) = (\pi/4, \pi/4)$ is consistent with the analyses of $V_{\mathbf{q}}$, as shown in Fig. 3(e). A similar diagonally striped phase was recently observed at $(\theta, \varphi) = (0.28\pi, \pi/4)$ for ^{168}Er dipolar bosonic atoms trapped on an optical lattice [12].

From now on in this section, we set again a cutoff on V up to second-nearest neighbor and let the dipole direction change in the presence of a nonzero onsite repulsion. Figures 16 and 19 (Appendix) show the configurations which the analyses of $V_{\mathbf{q}}$ suggest as the most likely ground states. By comparing the energy of the different classical states listed in the Appendix, we note from Eqs. (A6) that the last term in the energy of all phase-separated (tilted-PS) states vanish as $L \rightarrow \infty$, so that all the PS states become degenerate in the thermodynamic limit.

Let us now consider very weak dipolar interactions. In this $U \gg V$ limit, the Mott phase is the ground-state configuration for all directions (θ, φ) . As V is increased and $U/V < 5.33$, striped phases start forming around $(\theta = \pi/2)$, where attractive dipolar interactions are present along the \hat{x} (or \hat{y}) direction while still being repulsive along \hat{y} (or \hat{x}). This energetically favors stripes along \hat{x} (or \hat{y}), which we denote by XS (or YS); their regions of stability in the $\theta \times \varphi$ plane are shown in Fig. 6, for the different values of U/V considered, increasing in size as U/V decreases.

Increasing V further we reach $U/V = 2.71$ where a phase-separated phase [(PS), see illustration in Fig. 19] appears, as shown in Fig. 6(b), for $U/V = 2.67$. When $\theta \approx \pi/2$, the average dipolar interaction is attractive, and the phase-separated

states compete with both XS (YS) and the Mott state. For $\theta = \pi/2$, an XS-diagonally striped-PS transition takes place, with the intervening diagonally striped phase being small for this value of U/V . The PS state has the global minimum energy within the range $\varphi_{cx} < \varphi < \varphi_{cy}$, since the components of the dipolar interaction are attractive, i.e., $V_x, V_y, V_{d1} < 0$ (see their definition in the Appendix), thus favoring particle condensation. In this range of U/V , the PS competes with the Mott phase as the dipole direction deviates from $\theta = \pi/2$. The Mott-PS transition occurs in a horizontal line of the phase diagram whose critical value of θ is given by

$$\theta_{c1} = \arcsin \left[\pm \sqrt{\left(\frac{2}{3} + \frac{U}{3V} \frac{\sqrt{2}}{1+2\sqrt{2}} \right)} \right], \quad (7)$$

where \pm respectively correspond to the critical θ for $\theta < \pi/2$ and $\theta > \pi/2$; again, note that θ_{c1} is independent of φ . For $U/V > (1+2\sqrt{2})/\sqrt{2} \approx 2.71$, Eq. (7) yields $\sin \theta_{c1} > 1$ so that the PS phase is suppressed, with the Mott state dominating the whole region $\varphi_{cx} < \varphi < \varphi_{cy}$ of the phase diagram.

Figure 6(c), where $U/V = 2.22$, shows the presence of a cbCDW region. Starting from the isotropic case, $\theta = 0$, when the GS is the cbCDW configuration, the transition to the Mott state takes place at θ_{c2} , given by

$$\theta_{c2} = \arcsin \left[\pm \sqrt{\frac{2}{3} + \left(\frac{\sqrt{2}}{2-4\sqrt{2}} \right) \frac{2U}{3V}} \right], \quad (8)$$

where the \pm apply to $\theta_{c2} > \pi/2$ or $\theta_{c2} < \pi/2$, respectively. The cbCDW phase starts to form at $U/V = (4\sqrt{2}-2)/\sqrt{2} \approx 2.586$, as above this value θ_{c2} is complex. Within the atomic limit, θ_{c2} , separating the Mott and cbCDW phases, is independent of φ giving rise to the straight horizontal line phase boundaries in Fig. 6(c).

As U/V is reduced, as shown in Figs. 6(a)–6(d), one can observe a suppression of the Mott phase and the corresponding expansion of all other phases. As discussed in Figs. 5(a) and 5(c), $U \lesssim V$ leads to the formation of tilted CDW phases

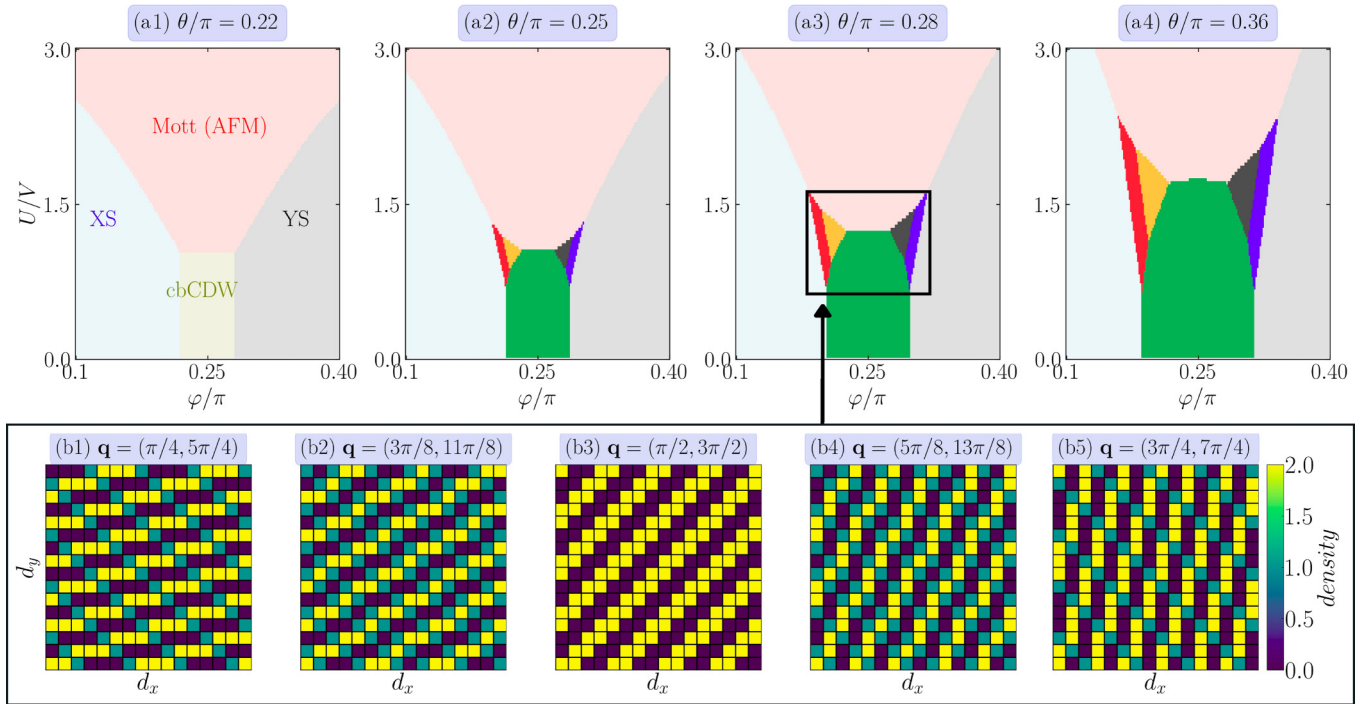


FIG. 7. Ground-state phase diagram in terms of U/V and φ/π obtained in the atomic limit. Panels (a1) to (a4) show phase diagrams for different values of θ in the regime of parameters that diagonally striped phases are energetically favored (see text). Panels (b1)–(b5) show the density profile of the 5 diagonally striped phases that are stabilized when the parameter φ increases for $\theta/\pi = 0.28$ and $L = 16$.

and strong suppression of the Mott phase. Figure 6(d) shows that for $U/V = 1$ different types of diagonally striped phases arise.

To better understand the nature and the formation of the diagonally striped phases, we analyze phase diagrams in the U/V versus φ/π plane in the regime where they are energetically favored within the atomic limit approximation, shown in Fig. 7. Starting from $\theta/\pi = 0.22$ [Fig. 7(a1)], a small increase in the polar angle, to $\theta/\pi = 0.25$ [Fig. 7(a2)] changes the ground state from a cbCDW to a tilted CDW phase around $\varphi/\pi = 0.25$ and $U/V \lesssim 1$, in agreement with Figure 6(d). Moving the azimuthal angle away from $\varphi/\pi = 0.25$ induces other diagonally striped phases, with density profiles and wave vectors \mathbf{q} shown in Figs. 7(b1)–7(b5). Tilting the polar angle further in the xy plane enhances the anisotropic nature of the dipolar interactions, expanding the range of the diagonally striped phases in the $(U/V, \varphi/\pi)$ parameter space. Consequently, the Mott phase shrinks and the XS and YS phases are pushed to smaller φ and φ/π closer to $1/2$, respectively. XS and YS phases become more stable at larger U/V , also collaborating to the reduction of the Mott phase. The box in Fig. 7(a3) highlights a region of the phase diagram where different phases are present. For $\theta/\pi = 0.28$, $U/V \approx 1.2$ marks the frontier between the Mott and tilted CDW phases around $\varphi/\pi = 0.25$. Sweeping φ/π will take the system to go through a cascade of phases: XS phase [with $\mathbf{q} = (0, \pi)$] $\rightarrow \mathbf{q} = (\pi/4, 5\pi/4) \rightarrow \mathbf{q} = (3\pi/8, 11\pi/8) \rightarrow \mathbf{q} = (\pi/2, 3\pi/2)$ (below $U/V = 1.2$) or Mott phase (above $U/V = 1.2$) $\rightarrow \mathbf{q} = (5\pi/8, 13\pi/8) \rightarrow \mathbf{q} = (3\pi/4, 7\pi/4) \rightarrow$ YS phase [with $\mathbf{q} = (\pi, 0)$]. In the Appendix, we show that longer-range dipolar interactions do

not change the nature of the tilted CDW states within this parameter regime. Instead, their effects on the phase diagram are quantitative. Specifically, while longer-range interactions energetically favor CDW phases over XS (or YS) phases, they do slightly broaden the region in the phase diagram where Mott states are stabilized.

One must comment on how these results are affected by a finite L . We recall [see Eqs. (A6)] that while the energies per particle in the atomic limit for the Mott, XS (or YS), and cbCDW states are independent of the system size, L , the PS states have contributions proportional to $1/L$, due to “interface” contributions [see Fig. 19]. Therefore, in a finite system, PS states with different orientations may be formed due to the anisotropic nature of the dipolar interaction. For instance, the strip in which the XPS (or YPS) phase is stable when $L \rightarrow \infty$ shrinks to a small lobe emerging from the striped phases when, say $L = 4$. By contrast, the boundaries involving non-PS phases are hardly affected by a finite L .

A parallel with recent experiments with magnetic Erbium atoms in an optical lattice [12] emulating the extended Bose-Hubbard is in order. Although the experiment was realized with hard-core bosons, where no double occupations are present, similar phases were identified, namely, checkerboard at $(\theta, \varphi) = (0, 0)$ and XS at $(\theta, \varphi) = (\pi/2, 0)$.

2. Perturbation theory— $t \ll V, U$

Let us now discuss how a small hopping ($t \ll V, U$) affects the atomic-limit phase diagrams, resorting to perturbation theory. The correction to the atomic-limit energies up to second-order perturbation theory, $E^{(2)}$, is described by the

effective Hamiltonian [51]

$$\langle \phi_0^i | \hat{\mathcal{H}}_{\text{eff}} | \phi_0^j \rangle = \langle \phi_0^i | \hat{K} | \phi_0^j \rangle + \sum_{m>0} \frac{\langle \phi_0^i | \hat{K} | \phi_m \rangle \langle \phi_m | \hat{K} | \phi_0^j \rangle}{E_0 - E_m}, \quad (9)$$

where E_m and $|\phi_m\rangle$ are the respective eigenvalues and eigenstates of $\hat{\mathcal{H}}_{\text{at}}$, $\hat{\mathcal{H}}_{\text{at}}|\phi_m\rangle = E_m|\phi_m\rangle$. $\hat{\mathcal{H}}_{\text{eff}}$ is therefore an operator which acts in the subspace of the degenerate ground states of $\hat{\mathcal{H}}_{\text{at}}$, $\{|\phi_0^i\rangle\}$, and the perturbation \hat{K} is the hopping term of the dipolar Hubbard model.

The correction $E^{(2)}$ is the lowest energy of $\hat{\mathcal{H}}_{\text{eff}}$. The cbCDW and the XS(YS) atomic-limit ground states form a subspace that is twofold degenerate in each case, so $\hat{\mathcal{H}}_{\text{eff}}$ is a 2×2 diagonal matrix. The diagonal term, $E^{(2)}$, is obtained by considering all possible processes described by the hopping term in Eq. (9) with certain intermediate states. For example, for the cbCDW configuration, this corresponds to states with one site breaking the checkerboard pattern, as shown in Fig. 2(d). The sum over all second-order processes then leads to a correction that scales with the number of sites,

$$\frac{E_{\text{cbCDW}}^{(2)}}{N} = \frac{2t^2}{U - 4V_x - 3V_y + 4V_{d1} + 4V_{d2}} + \frac{2t^2}{U - 4V_y - 3V_x + 4V_{d1} + 4V_{d2}}, \quad (10)$$

and

$$\frac{E_{\text{XS(YS)}}^{(2)}}{N} = \frac{2t^2}{U + 4V_{x(y)} - 3V_{y(x)} - 4V_{d1} - 4V_{d2}} \quad (11)$$

for the XS(YS) states. The typical intermediate states $|\phi_m\rangle$ associated with the XS ground state is also illustrated in Fig. 2(d). On the other hand, the atomic-limit Mott states form a macroscopically degenerate subspace, and $\hat{\mathcal{H}}_{\text{eff}}$ becomes an anisotropic SU(2) Heisenberg Hamiltonian [51,52]

$$\hat{\mathcal{H}}_{\text{eff}} = J_x \sum_i \hat{S}_i \cdot \hat{S}_{i\pm\hat{x}} + J_y \sum_i \hat{S}_i \cdot \hat{S}_{i\pm\hat{y}} - \frac{N}{4}(J_x + J_y), \quad (12)$$

where the exchange couplings $J_x = 4t^2/(U - V_x)$ and $J_y = 4t^2/(U - V_y)$ depend on the dipolar angles θ and φ . For J_x and $J_y > 0$, the ground state of $\hat{\mathcal{H}}_{\text{eff}}$ exhibits an antiferromagnetic order [63]. Here we use linear spin-wave theory [64] to determine the ground-state energy of $\hat{\mathcal{H}}_{\text{eff}}$, $E_{\text{MottAFM}}^{(2)}$, for different values of θ and φ .

By comparing the second-order energies,

$$E_{\text{Mott}} = E_{\text{Mott}}^{(0)} + E_{\text{Mott}}^{(2)}, \quad (13)$$

$$E_{\text{cbCDW}} = E_{\text{cbCDW}}^{(0)} + E_{\text{cbCDW}}^{(2)}, \quad (14)$$

and

$$E_{\text{XS(YS)}} = E_{\text{XS(YS)}}^{(0)} + E_{\text{XS(YS)}}^{(2)}, \quad (15)$$

we have established that the main effect of the hopping is to enlarge the region dominated by the Mott phase in the $\theta \times \varphi$ diagram; see Fig. 2(d). The critical angle θ_{c2} associated with the Mott-cbCDW transition decreases in comparison with the atomic-limit case. Further, due to the presence of anisotropic AFM correlations, θ_{c2} acquires a small dependence on φ , as can be seen from Fig. 8(b); that is, the effect of finite hopping

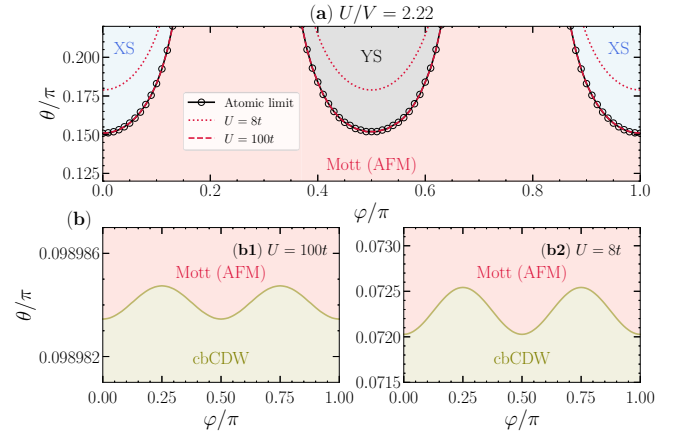


FIG. 8. Panel (a) shows how the XS(YS)-MottAFM transition lines are affected in second-order perturbation theory for $U = 100t$ (full red lines) and $U = 8t$ (dashed red lines). Results for the atomic limit are also presented. Panels (b) show the results for the cbCDW-MottAFM transition for $U/t = 100$ (b1) and $U/t = 8$ (b2).

is to introduce oscillations of negligible amplitudes on the border between the cbCDW and Mott phases. In addition, the lobes of the $\theta \times \varphi$ phase diagram dominated by the XS and YS phases shrink as we decrease the value of U to $U/t = 8$; see Fig. 8(a).

3. Lanczos results— $U = 8t$

We now turn to the correlation functions computed with the Lanczos method for $U = 8t$. Figure 9 shows spin and density correlation functions for $\theta = \pi/4$ as a function of φ/π obtained by means of Lanczos diagonalization. The ground state goes from the XS to the Mott phase around $\varphi/\pi = 0.12$ and then to YS phase at $\varphi/\pi = 0.38$, which is consistent with the $t = 0$ phase diagram presented in Fig. 6. Figures 10(a2) and 10(b2) show that for the XS (YS) phase $C_m(1, 0)$ [$C_m(0, 1)$] is nonzero whereas $C_m(0, 1)$ [$C_m(1, 0)$] remains zero, therefore moment-moment correlations alone can distinguish these two phases. For the cbCDW and Mott phases, however, both $C_m(1, 0)$ and $C_m(0, 1)$ are nonzero, one can resort to the local moment to separate between these two phases. For the transitions occurring as one varies φ for fixed $\theta = \pi/4$, Fig. 10(a1) shows that the local moment (m^2) is close to saturation in the Mott phase, but sharply decreases in the striped phases; a similar behavior occurs as θ varies

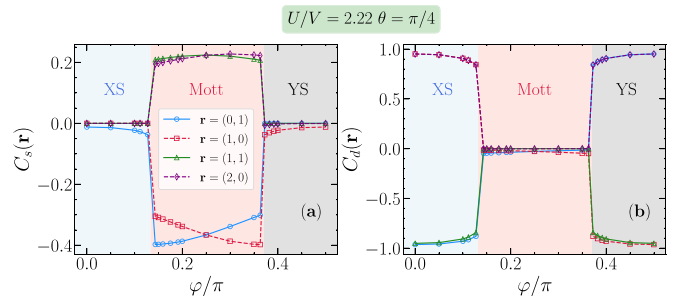


FIG. 9. Lanczos data for the dependence of (a) spin and (b) density correlation functions with φ for $U = 8t$, $V = 3.6t$, and $\theta = \pi/4$.

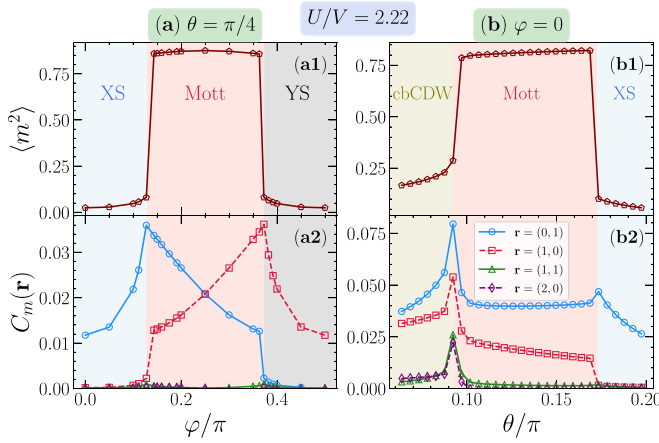


FIG. 10. Dependence of the local moment and moment-moment correlations with the angle (a) φ for $\theta = \pi/4$ and (b) θ for $\varphi = 0$. In both cases, we consider $U/V \simeq 2.22$ [$U = 8t$, $V = 3.6$]. The results are obtained with Lanczos diagonalization. Panel (b2) reproduces Fig. 2(c3) for a better understanding of the results.

with fixed φ , as in Fig. 10(b1). Thus, a combination of local moment and moment-moment correlations can determine the nature of the phases. By contrast, Figs. 10(a2) and 10(b2) [or Fig. 2(c3)] show that $C_m(\mathbf{r})$ is peaked at the different transitions for some specific directions \mathbf{r} . Thus, the sharp drop in the local moment is responsible for the sharpness of $C_m(\mathbf{r})$ at the transition. Although analyzing the local moment and moment-moment correlations allows one to discern the different phases at play, the changes in the values of the moment-moment correlation that mark the phase transitions might not be large enough to be experimentally detectable.

However, density correlations present sign changes and have been successfully used to identify different phases in recent experiments with dipolar bosons [12]. Figure 11 presents color maps of the density-density correlation function for $U/t = 8$ and $V/t = 3.6$ calculated at representative angles. For isotropic interactions ($\theta = \varphi = 0$), shown in Fig. 11(a), the pattern clearly shows that the system is in the checkerboard phase. The cbCDW phase is the one where density correlations show stronger dependence on V/t [Fig. 2(a2)] and

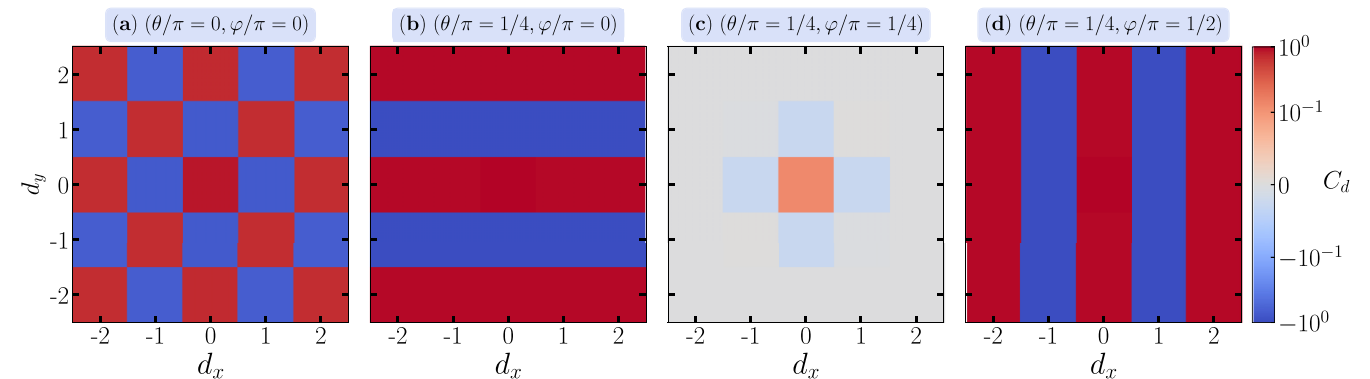


FIG. 11. Contour plots for the density-density correlation function obtained through Lanczos diagonalization for $U/t = 8$, $V/t = 3.6$, for $(\theta/\pi, \varphi/\pi) = (0, 0)$ (a), $(1/4, 0)$ (b), $(1/4, 1/4)$ (c), and $(1/4, 1/2)$. Colors are arranged in a symmetric logarithmic scale around zero wherein a linear scale is drawn between the values ± 0.1 .

dipole orientation [Fig. 2(c2)], nonetheless it is the only case with a positive value of $C_d(1, 1)$, as well as negative values of both $C_d(1, 0)$ and $C_d(0, 1)$. The Mott state is characterized by small density-density correlation functions for all distances, as shown in Figs. 2(a2), 2(b2), and 2(c2), in Fig. 9(b), and also in the contour plot shown in Fig. 11(c).

The XS and YS phases present positive values of $C_d(2, 0)$ and negative values of $C_d(1, 1)$, with the XS (YS) phase presenting $C_d(1, 0) > 0$ ($C_d(1, 0) < 0$) and $C_d(0, 1) < 0$ ($C_d(0, 1) > 0$). Figures 2(b2) and 2(c2) and Fig. 9(b) show that whenever striped phases are formed, density correlations approach their saturation value $C_d = \pm 1$. Figures 11(b) and 11(d) show the contour plots for systems in YS and XS phases, respectively.

IV. THERMAL TRANSITIONS

Having characterized the ground-state phases and their transitions in terms of the dipole orientations and magnitude of the interactions, an important question, refers to the robustness of these phases in the presence of thermal fluctuations.

To estimate the critical temperatures T_c^α signaling the onset of the different ordered classical phases, α , listed in Eq. (A6), we use the parallel tempering [53] (or replica exchange method) of the atomic Hamiltonian, Eq. (A1). In summary, we use a Monte Carlo (MC) sampling of the occupations of both species $\{\uparrow$ and $\downarrow\}$, promoting random swaps of site occupancies, complemented by random creation and destruction of particles at different temperatures. These moves are implemented to obey the detailed balance condition in a particle-hole symmetric version of Eq. (A1). This guarantees that, on average, one keeps $\langle \hat{n}_\uparrow \rangle = \langle \hat{n}_\downarrow \rangle = 0.5$. After a single MC sweep, an attempt to swap the configurations related to adjacent temperatures in a given range is induced and accepted with a probability

$$p = \min\{1, \exp[-(\beta_i - \beta_j)(E_j - E_i)]\}, \quad (16)$$

where $\beta_i = 1/T_i$ is the inverse temperature of a given configuration i whose associated energy for the Hamiltonian (A1) is E_i . Approaches like this have been extensively used to obtain the ground state of models in which the free-energy

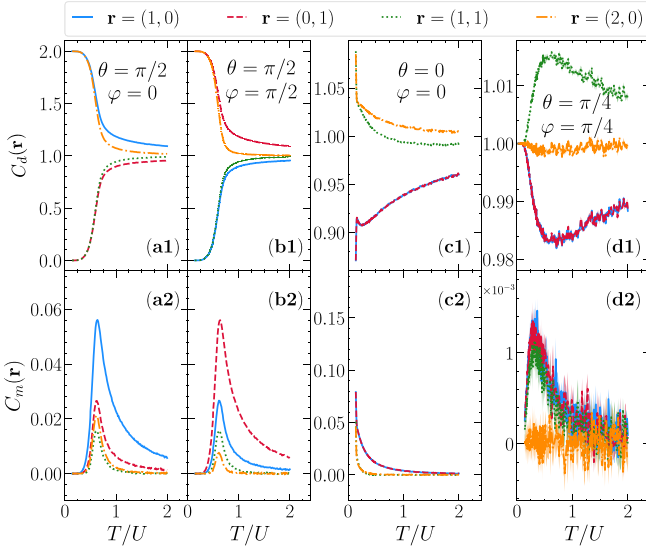


FIG. 12. Parallel tempering data for density-density (top panels) and moment-moment (bottom panels) correlation functions as a function of temperature for (a) $\theta = \pi/2$ and $\varphi = 0$ (XS phase), (b) $\theta = \varphi = \pi/2$ (YS phase), (c) $\theta = \varphi = 0$ (cbCDW phase) and (d) $\theta = \varphi = \pi/4$ (Mott phase). Data are for 8×8 lattices with $U = 8$ and $U/V = 2.22$.

landscape is rough, i.e., with many local minima. A canonical example of such a scenario is of frustrated disordered spin systems as given for the disordered classical Ising model used to understand spin glass physics [65,66].

We typically use square lattices up to $L = 32$, and 20 000 MC sweeps, with approximately 300 different temperatures chosen in a way to ensure that the range encompasses the associated critical temperatures T_c^α . A known difficulty of the parallel tempering scheme is choosing the optimal set of temperatures [65,67,68], which overcome the trapping of metastable configurations when $T \rightarrow 0$. Although sub-optimal, we used a simple approach of evenly spaced ones, which is more than sufficient to resolve the critical temperatures associated with the onset of the different phases.

Similarly to the quantum version of the Hamiltonian, Eq. (1), we present local correlations $[C_d(\mathbf{r})$ and $C_m(\mathbf{r})]$ which help to identify the density distribution in all classical phases. Figure 12 shows the temperature dependence of the density-density and moment-moment correlation functions for different polarization directions obtained through parallel tempering.

As expected, the density correlations start at their ground-state values consistent with XS and YS phases [Figs. 12(a1) and 12(b1), respectively], and decrease in magnitude as T increases. An estimate of the temperature scale marking the onset of the ordered phases can be obtained from the peak position of the moment-moment correlations, shown in Figs. 12(a2) and 12(b2): they are the same for both XS and YS phases, namely, $T_c^{\text{XS}}/U = T_c^{\text{YS}}/U \simeq 0.61$, for $U/V = 2.22$. For these values of U and V , we estimate from Figs. 12(c1) and 12(c2) the ordering temperature for the cbCDW phase as $T/U \sim 0.1$, which lies in a range in parallel tempering simulations which are hindered by trapped metastable configurations.

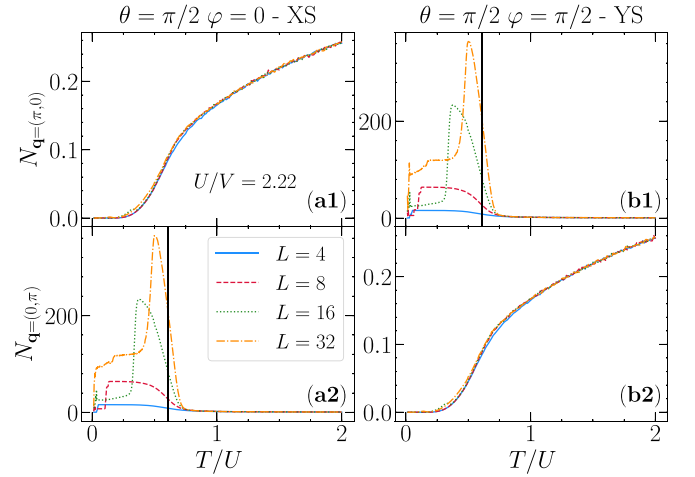


FIG. 13. Temperature dependence of the density structure factor for the stripe phases XS in (a) and YS in (b) obtained via parallel tempering of the atomic-limit Hamiltonian. We select two channels with $\mathbf{q} = (\pi, 0)$ in (a1) and (b1), whereas (a2) and (b2) display the $\mathbf{q} = (0, \pi)$ results. Vertical lines depict the peak position of the temperature-dependent moment-moment correlations, signaling the thermal transition. We fix the interaction ratio $U/V = 2.22$.

Nonetheless, we can infer an upper bound $T_c^{\text{cbCDW}} < T_c^{\text{XS}}$, which is valid for different values of the ratio $U/V (< 5.33)$. One can understand this result by noticing that charge gaps are larger for the striped phases than for the cbCDW phase, thus leading to higher critical temperatures.

Finally, for polarizations leading to the Mott phase, such as $\theta = \varphi = \pi/4$ shown in Figs. 12(d1) and 12(d2), the atomic limit also displays a critical temperature associated with the onset of a homogeneous density ordering, though without any manifest spin order, which is absent in this regime due to the vanishing exchange couplings when $t \rightarrow 0$.

To complement this analysis and describe a fully developed order, we also compute the associated density structure factor,

$$N_{\mathbf{q}} = \frac{1}{L^2} \left\langle \sum_{i,j} e^{i\mathbf{q} \cdot (i-j)} \hat{n}_i \hat{n}_j \right\rangle_{\text{MC}}, \quad (17)$$

which becomes an extensive quantity in the presence of a given charge order with wave-vector \mathbf{q} , and is also used to characterize different phases in experiments [12].

As an example, we report in Fig. 13 the comparison of $N_{\mathbf{q}}$ for two striped phases, XS ($\theta = \pi/2$ and $\phi = 0$) and YS ($\theta = \phi = \pi/2$) in Figs 13(a) and 13(b), respectively. We note that the structure factor has a symmetric role for different channels: while for XS the $\mathbf{q} = (0, \pi)$ channel displays an extensive behavior at low temperatures, $\mathbf{q} = (\pi, 0)$ reflects this corresponding behavior for the YS phase. For very low temperatures, however, the aforementioned trapping of metastable configurations occurs, preventing the observation of a fully formed plateau; this, in turn, signals that the correlation length for this ordering has reached the linear size of the system. Nonetheless, the critical temperatures T_c^{XS} and T_c^{YS} lie well above the temperatures where these problems begin to occur. As an estimation, we also display as

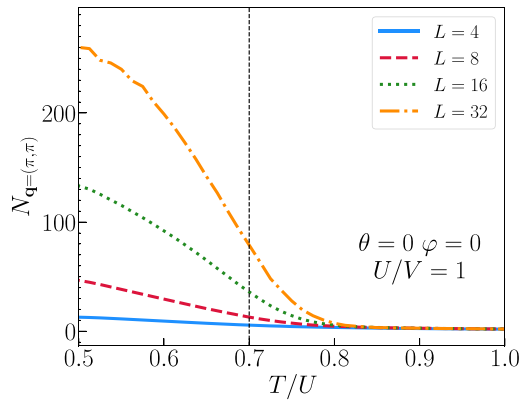


FIG. 14. Temperature dependence of the $\mathbf{q} = (\pi, \pi)$ density structure factor for $\hat{\mathbf{z}}$ oriented dipoles. The extensive behavior at low temperatures signals the onset of the cbCDW order. As before, the vertical line depicts the peak position of the temperature-dependent moment-moment correlation functions. We choose the ratio of interactions $U/V = 1$.

a vertical line in these panels the thermal peak-positions of the moment-moment correlation functions (as in Fig. 12), which are very close to the regime where the curves for different system sizes start displaying an extensive behavior. Conversely, for the channels $\mathbf{q} = (\pi, 0)$ [Fig. 13(a1)] and $\mathbf{q} = (0, \pi)$ [Fig. 13(b2)] for the XS and YS phases, respectively, $N_{\mathbf{q}}$ is approximately independent of the system size, thus confirming the nature of the density periodicity. Last, we performed similar parallel tempering simulations for the case of isotropic interactions, i.e., $\theta = \varphi = 0$, where the ground state of Eq. (A1) displays cbCDW order. Figure 14 shows the temperature dependence of the $\mathbf{q} = (\pi, \pi)$ channel for the density structure factor: As for the stripe phases, this quantity displays an extensive onset at low temperatures, which is close to the peak position of the corresponding moment-moment correlations, thus signaling the checkerboard nature of the density distribution.

Summing up, the estimates for the critical temperatures for the ordering of the XS, YS and cbCDW phases are gathered in Fig. 15; they clearly show that the striped phases are more robust, with higher critical temperatures than the cbCDW phase for all U/V . We recall that for $U/V > 5.33$ the ground state is a Mott “insulator” for all polarization directions.

V. SUMMARY

We have established that dipolar fermionic atoms in an optical lattice provide a setup in which Mott and density-wave states can be stabilized by controlling the direction of polarization. These density-wave states may be anisotropic (stripelike) or occupy one of the sublattices; in addition, one may also find anisotropic phase-separated phases. Depending on the strength of the dipolar interaction and on the polar angle, a rotation of the polarization around the $\hat{\mathbf{z}}$ axis can switch between the density-wave states through a succession of diagonally striped phases. Our results are based on exact diagonalizations of a dipolar Fermi-Hubbard Hamiltonian on a 4×4 lattice at half-filling, in the regime of strong onsite re-

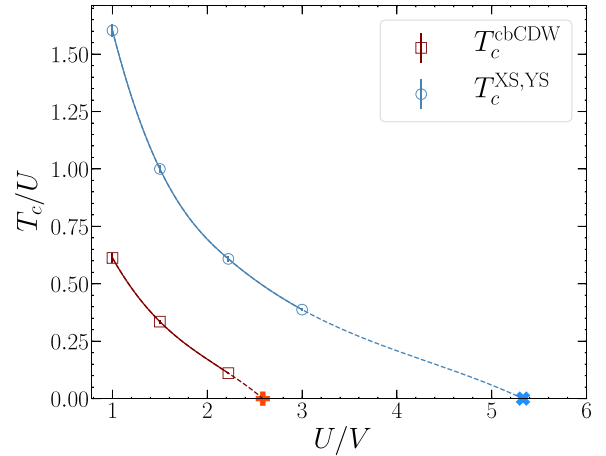


FIG. 15. Critical temperature for the XS ($\theta = \pi/2$, $\varphi = 0$), YS ($\theta = \varphi = \pi/2$) and cbCDW ($\theta = \varphi = 0$) phases as a function of U/V . Filled markers at $T = 0$ denote the atomic limit results when $L \rightarrow \infty$ (see Sec. III), associated with the onset of the Mott insulating phase for the corresponding dipole orientations.

pulsion. In this regime, finite-size effects are not too drastic, as evidenced by the comparison with predictions obtained in the atomic limit (hopping $t \rightarrow 0$), aided by simulated annealing. The use of moment-moment [54–57] and density-density [12] correlations have proven to be powerful tools to probe different phases in experiments with ultracold atoms so that our theoretical predictions for these quantities should provide guidance in the experimental search for these phases with fermionic atoms.

Recent experiments with bosonic dipolar atoms at half-filling [12] found striped and checkerboard phases for the same dipole orientation as the ones obtained here. These similarities between the density patterns in bosonic and fermionic systems can be justified, to some extent, by the fact that the experiments were carried out under the constraint of hard-core bosons (i.e., site occupations 0 or 1). On the other hand, the spin degrees of freedom may favor an AFM phase over one with accumulated atoms along the diagonals, as observed in Ref. [12].

ACKNOWLEDGMENTS

Financial support from Fundação Carlos Chagas Filho de Amparo à Pesquisa do Estado do Rio de Janeiro Grants No. E-26/200.959/2022 and No. E-26/210.100/2023 (T.P.), and No. E.26/202.965/2017 (R.R.d.S.); CNPq Grants No. 403130/2021-2 and No. 308335/2019-8 (T.P.) is gratefully acknowledged. We also acknowledge support from INCT-IQ and CAPES. R.M. acknowledges support from the NSFC Grants No. NSAF-U2230402, No. 12111530010, No. 12222401, and No. 11974039. Numerical simulations were performed in the Tianhe-2JK at the Beijing Computational Science Research Center. T.M.S., T.P., and R.R.d.S. are also grateful to CSRC for the hospitality while this work was concluded. T.M.S. acknowledges support by the European Research Council (ERC) under the European Unions Horizon

2020 research and innovation programme (Grant Agreement No. 853443).

APPENDIX: ATOMIC LIMIT

In this Appendix, we provide additional results of the dipolar Hubbard model in the atomic limit ($t = 0$),

$$\hat{\mathcal{H}}_{\text{at}} = U \sum_{\mathbf{i}} \hat{n}_{\mathbf{i}\uparrow} \hat{n}_{\mathbf{i}\downarrow} + \sum_{\mathbf{i} \neq \mathbf{j}} V_{\mathbf{ij}} \hat{n}_{\mathbf{i}} \hat{n}_{\mathbf{j}}, \quad (\text{A1})$$

where up to next-nearest neighbors $V_{\mathbf{ij}}$ becomes

$$V_x \equiv V(1 - 3 \sin^2 \theta \cos^2 \varphi), \quad (\text{A2})$$

$$V_y \equiv V(1 - 3 \sin^2 \theta \sin^2 \varphi), \quad (\text{A3})$$

$$V_{d1} \equiv \frac{V}{2^{3/2}} \left[1 - \frac{3}{2} \sin^2 \theta (1 + \sin 2\varphi) \right], \quad (\text{A4})$$

$$V_{d2} \equiv \frac{V}{2^{3/2}} \left[1 - \frac{3}{2} \sin^2 \theta (\cos 2\varphi + \sin 2\varphi) \right]. \quad (\text{A5})$$

We have considered the atomic limit on $L \times L$ lattices so that the range of interactions can be extended to neighbors

separated by up to $\sim L/2$; due to the periodic boundary conditions, sites separated by a distance larger than this limit would actually be nearer. We have checked that taking $L = 40$ is sufficient to highlight the most significant charge-ordered phases and that the interactions beyond $L \sim 40$ hardly change the patterns.

The eigenstates of Eq. (A1) are product states (classical states), and the ground state (GS) is the one which minimizes the energy for the given values of U , V , θ , and φ . For instance, when $U \gg V$, double occupancies are suppressed due to the high-energy penalty U , and the GS corresponds to a Mott insulator. Physical intuition together with analyses of the Fourier transform of the dipolar potential can be used to set up other possible GS classical states; see, e.g., Figs. 2, 16, and 19.

To illustrate how we set up the different classical states considered in this work, we consider as an example the case in which the dipoles are at $\theta = \pi/4$ and $0.1 < \varphi/\pi < 0.35$. In this regime of parameters, the analysis of the Fourier transform of $V_{i,j}$ suggests that CDW-ordered phases characterized by multiple wave vectors (i.e., \mathbf{q}_{min} , see Fig. 4) can be stabilized as the ground state of Eq. (A1). The ordered states are built in such a way that they are characterized by an extensive density structure factor, $N_{\mathbf{q}}$, at the channel \mathbf{q} . Figure 16 shows

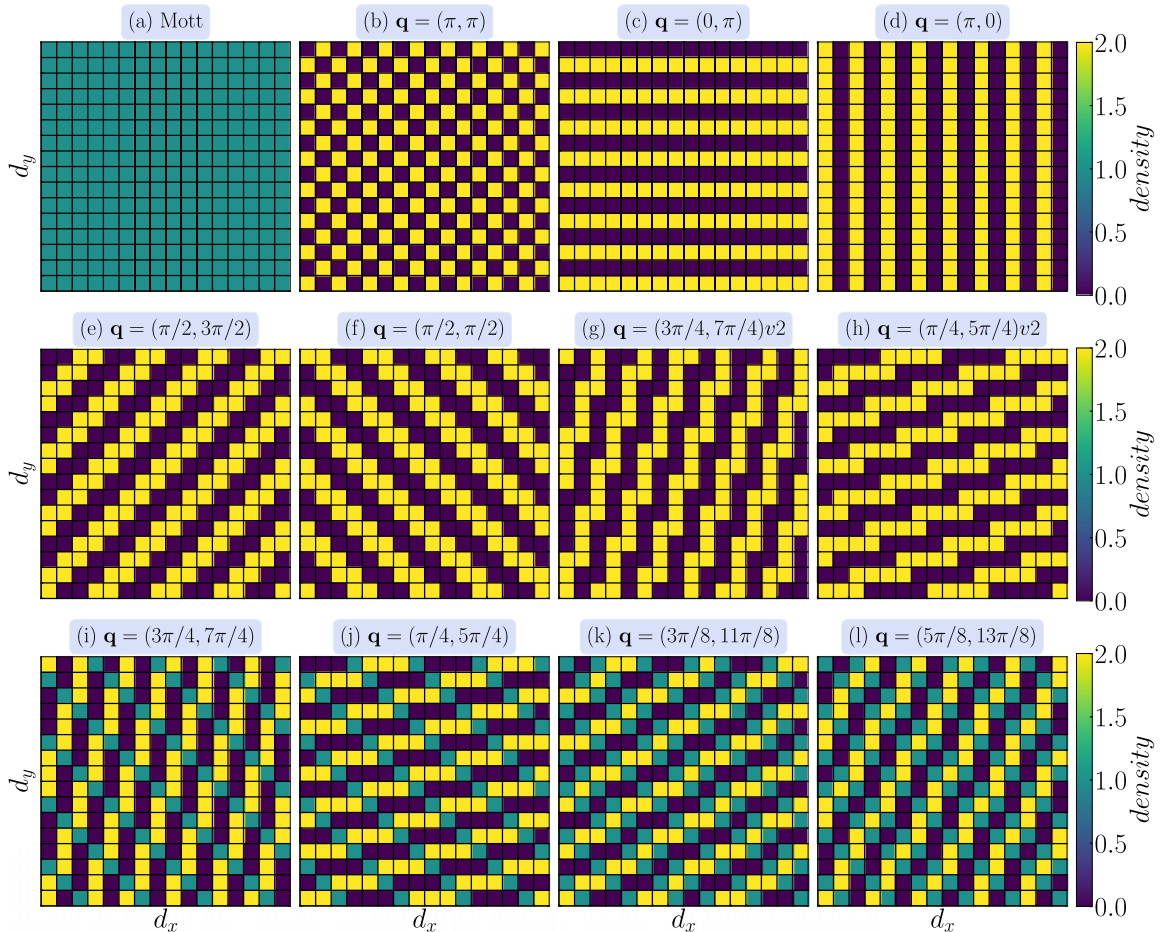


FIG. 16. Panels (a)–(m) show the spatial density profile of the ordered phases considered in this work. The phases are labeled by the wave vector \mathbf{q} defining the dominant density structure factor, $N_{\mathbf{q}}$ [see Eq. (17)].

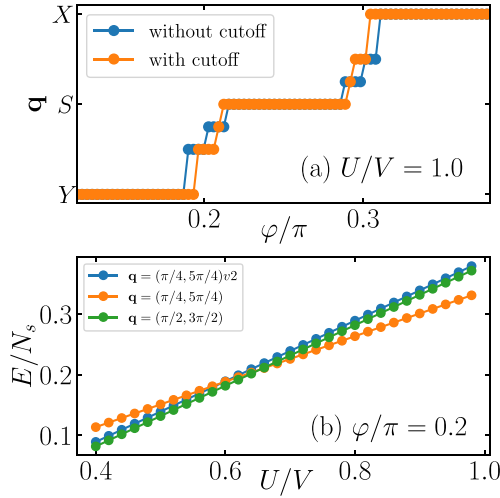


FIG. 17. Panel (a) shows the characteristic wave-vector, \mathbf{q} , of the ground state as a function of φ for $U/V = 1$; we plot the values of \mathbf{q} along the path $Y = (0, -\pi) \rightarrow S = (-\pi/2, -\pi/2) \rightarrow X = (\pi, 0)$ of the first Brillouin zone. We consider the cases in which the range of dipolar interactions are cutoff: up to second nearest-neighbors (with cutoff) and up to $L/2$ (without cutoff). Panel (b) shows the energy of some diagonally striped phases as a function of U/V for $\varphi/\pi = 0.2$, the corresponding ordered phases are illustrated in Fig. 16. We consider $\theta/\pi = 0.28$ and $L = 16$ in both panels.

some ordered phases for unit cell $L = 16$; see, in particular, Figs. 16(e)–16(m).

By comparing the energies of the different configurations, we establish the phase diagrams presented in Figs. 6 and 7. As a complement to the discussion in Sec. III B 1, we analyze the effect of the dipolar interaction's long-range nature in stabilizing the diagonally striped phases. Figure 17(a) shows how the characteristic wave-vector \mathbf{q} of the GS evolves with φ for the cases in which the interactions are (i) cut off up to the second nearest-neighbor and (ii) the entire range is considered. The results show that the longer-range interaction barely affects the stabilization of the diagonally striped phases; see Fig. 18.

Further, we analyze the effect of the onsite interaction U by comparing the energy of different diagonally striped phases in Fig. 17(b). For the state characterized by $\mathbf{q} = (\pi/4, 5\pi/4)$, we consider two possible density arrangements: one in which all sites are either empty or doubly occupied and one in which the ordered phase is characterized by empty, singly, and doubly occupied sites; see Figs. 16(h) and 16(j), respectively. For larger values of the onsite interaction (i.e., $U/V \gtrsim 0.6$), the ordered phase characterized by a pattern containing empty, doubly, and (also) singly occupied sites have the lower energy, as discussed in Sec. III B 1.

Finally, we present below the energies per particle at half-filling (considering a cutoff up to second nearest-neighbor sites) for the competing ground states for an $L \times L$ lattice with periodic boundary conditions

$$\frac{E_0^{\text{cbCDW}}}{L^2} = \frac{U}{2} + 2(V_{d1} + V_{d2}), \quad (\text{A6a})$$

$$\frac{E_0^{\text{Mott}}}{L^2} = V_x + V_y + V_{d1} + V_{d2}, \quad (\text{A6b})$$

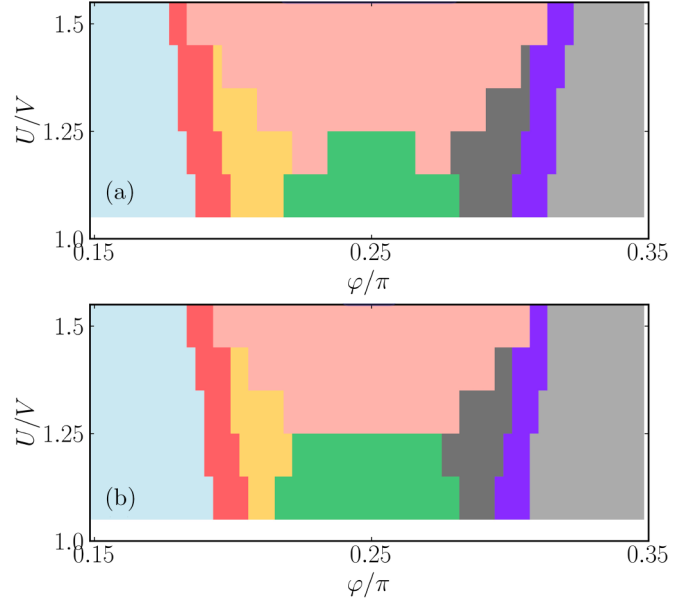


FIG. 18. Panels (a) and (b) show the ground-state phase diagram in terms of U/V and φ/π obtained in the atomic limit for the cases: (a) without a cutoff and (b) with a cutoff up to the second nearest-neighbors in the dipolar interactions. Color code for the different phases follows the one in Fig. 7, and parameters are $\theta/\pi = 0.28$ and $L = 16$.

$$\frac{E_0^{\text{XS}}}{L^2} = \frac{U}{2} + 2V_x, \quad (\text{A6c})$$

$$\frac{E_0^{\text{YS}}}{L^2} = \frac{U}{2} + 2V_y, \quad (\text{A6d})$$

$$\frac{E_0^{\text{d1S}}}{L^2} = \frac{U}{2} + (V_x + V_y + 2V_{d1}), \quad (\text{A6e})$$

$$\frac{E_0^{\text{d2S}}}{L^2} = \frac{U}{2} + (V_x + V_y + 2V_{d2}), \quad (\text{A6f})$$

$$\frac{E_0^{\text{d3S}}}{L^2} = \frac{3U}{8} + \left(\frac{3V_x}{2} + \frac{V_y}{2} + V_{d1} + \frac{V_{d2}}{4} \right), \quad (\text{A6g})$$

$$\frac{E_0^{\text{d4S}}}{L^2} = \frac{3U}{8} + \left(\frac{V_x}{2} + \frac{3V_y}{2} + V_{d1} + \frac{V_{d2}}{4} \right), \quad (\text{A6h})$$

$$\frac{E_0^{\text{d5S}}}{L^2} = \frac{5U}{16} + \left(\frac{3V_x}{4} + \frac{5V_y}{4} + \frac{11V_{d1}}{8} + \frac{3V_{d2}}{8} \right), \quad (\text{A6i})$$

$$\frac{E_0^{\text{d6S}}}{L^2} = \frac{5U}{16} + \left(\frac{5V_x}{4} + \frac{3V_y}{4} + \frac{11V_{d1}}{8} + \frac{3V_{d2}}{8} \right), \quad (\text{A6j})$$

$$\frac{E_0^{\text{xPS}}}{L^2} = \frac{U}{2} + 2(V_x + V_y + V_{d1} + V_{d2}) \quad (\text{A6k})$$

$$-\frac{1}{L}4(V_y + V_{d1} + V_{d2}), \quad (\text{A6l})$$

$$\frac{E_0^{yPS}}{L^2} = \frac{U}{2} + 2(V_x + V_y + V_{d1} + V_{d2}) \quad (\text{A6m})$$

$$-\frac{1}{L}4(V_x + V_{d1} + V_{d2}), \quad (\text{A6n})$$

$$\frac{E_0^{d1PS}}{L^2} = \frac{U}{2} + 2(V_x + V_y + V_{d1} + V_{d2}) \quad (\text{A6o})$$

$$-\frac{1}{L}4(V_x + V_y + 2V_{d2}), \quad (\text{A6p})$$

$$\frac{E_0^{d2PS}}{L^2} = \frac{U}{2} + 2(V_x + V_y + V_{d1} + V_{d2}) \quad (\text{A6q})$$

$$-\frac{1}{L}4(V_x + V_y + 2V_{d1}), \quad (\text{A6r})$$

where xPS and yPS denote \hat{x} - and \hat{y} -oriented phase-separated states [Fig. 19], the energies d1S and d2S correspond to the configuration shown in Figs. 16(e) and 16(f), respectively, while energies dS3-6S correspond to the configurations shown in Figs. 16(i)–16(m). Last, d1PS and d2PS denote $\pm\pi/4$ -oriented phase-separated states; see bottom panels in Fig. 19.

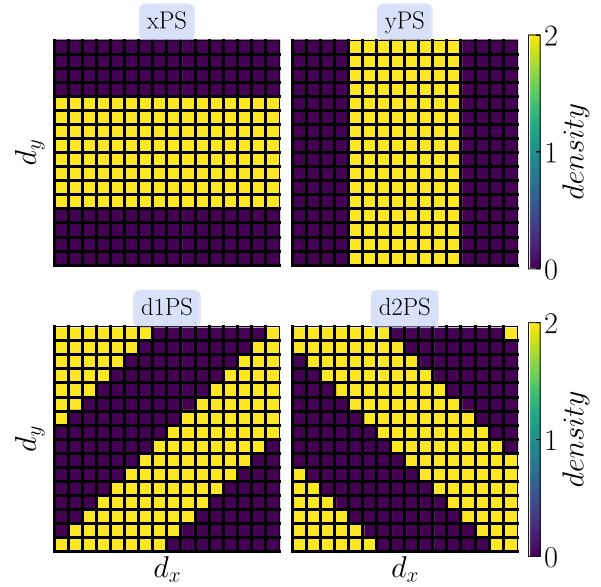


FIG. 19. Some phase-separated (PS) configurations for a 16×16 lattice.

-
- [1] D. Jaksch and P. Zoller, The cold atom Hubbard toolbox, *Annu. Phys.* **315**, 52 (2005).
- [2] I. Bloch, J. Dalibard, and W. Zwerger, Many-body physics with ultracold gases, *Rev. Mod. Phys.* **80**, 885 (2008).
- [3] T. Esslinger, Fermi-Hubbard physics with atoms in an optical lattice, *Annu. Rev. Condens. Matter Phys.* **1**, 129 (2010).
- [4] D. C. McKay and B. DeMarco, Cooling in strongly correlated optical lattices: Prospects and challenges, *Rep. Prog. Phys.* **74**, 054401 (2011).
- [5] L. D. Carr, D. DeMille, R. V. Krems, and J. Ye, Cold and ultracold molecules: Science, technology, and applications, *New J. Phys.* **11**, 055049 (2009).
- [6] T. Lahaye, C. Menotti, L. Santos, M. Lewenstein, and T. Pfau, The physics of dipolar bosonic quantum gases, *Rep. Prog. Phys.* **72**, 126401 (2009).
- [7] C. Trefzger, C. Menotti, B. Capogrosso-Sansone, and M. Lewenstein, Ultracold dipolar gases in optical lattices, *J. Phys. B: At. Mol. Opt. Phys.* **44**, 193001 (2011).
- [8] B. Gadway and B. Yan, Strongly interacting ultracold polar molecules, *J. Phys. B: At. Mol. Opt. Phys.* **49**, 152002 (2016).
- [9] Y. Bao, S. S. Yu, L. c Anderegge, E. Chae, W. Ketterle, K.-K. Ni, and J. M. Doyle, Dipolar spin-exchange and entanglement between molecules in an optical tweezer array, *arXiv:2211.09780*.
- [10] S. Baier, D. Petter, J. H. Becher, A. Patscheider, G. Natale, L. Chomaz, M. J. Mark, and F. Ferlaino, Realization of a strongly interacting fermi gas of dipolar atoms, *Phys. Rev. Lett.* **121**, 093602 (2018).
- [11] M. A. Norcia and F. Ferlaino, Developments in atomic control using ultracold magnetic lanthanides, *Nat. Phys.* **17**, 1349 (2021).
- [12] L. Su, A. Douglas, M. Szurek, R. Groth, S. Furkan Ozturk, A. Krahn, A. H. Hébert, G. A. Phelps, S. Ebadi, S. Dickerson, F. Ferlaino, O. Marković, and M. Greiner, Dipolar quantum solids emerging in a Hubbard quantum simulator, *Nature* **622**, 724 (2023).
- [13] A. Griesmaier, J. Werner, S. Hensler, J. Stuhler, and T. Pfau, Bose-Einstein condensation of chromium, *Phys. Rev. Lett.* **94**, 160401 (2005).
- [14] A. Frisch, M. Mark, K. Aikawa, S. Baier, R. Grimm, A. Petrov, S. Kotochigova, G. Quéméner, M. Lepers, O. Dulieu, and F. Ferlaino, Ultracold dipolar molecules composed of strongly magnetic atoms, *Phys. Rev. Lett.* **115**, 203201 (2015).
- [15] M. Lu, N. Q. Burdick, and B. L. Lev, Quantum degenerate dipolar Fermi gas, *Phys. Rev. Lett.* **108**, 215301 (2012).
- [16] K. Aikawa, S. Baier, A. Frisch, M. Mark, C. Ravensbergen, and F. Ferlaino, Observation of Fermi surface deformation in a dipolar quantum gas, *Science* **345**, 1484 (2014).
- [17] K.-K. Ni, S. Ospelkaus, M. H. G. de Miranda, A. Pe'er, B. Neyenhuis, J. J. Zirbel, S. Kotochigova, P. S. Julienne, D. S. Jin, and J. Ye, A high phase-space-density gas of polar molecules, *Science* **322**, 231 (2008).
- [18] A. Chotia, B. Neyenhuis, S. A. Moses, B. Yan, J. P. Covey, M. Foss-Feig, A. M. Rey, D. S. Jin, and J. Ye, Long-lived dipolar molecules and Feshbach molecules in a 3D optical lattice, *Phys. Rev. Lett.* **108**, 080405 (2012).
- [19] M. Baranov, Theoretical progress in many-body physics with ultracold dipolar gases, *Phys. Rep.* **464**, 71 (2008).
- [20] M. A. Baranov, M. Dalmonte, G. Pupillo, and P. Zoller, Condensed matter theory of dipolar quantum gases, *Chem. Rev.* **112**, 5012 (2012).
- [21] A. de Paz, A. Sharma, A. Chotia, E. Maréchal, J. H. Huckans, P. Pedri, L. Santos, O. Gorceix, L. Vernac, and B. Laburthe-Tolra, Nonequilibrium quantum magnetism in a dipolar lattice gas, *Phys. Rev. Lett.* **111**, 185305 (2013).

- [22] B. Yan, S. A. Moses, B. Galway, J. P. Covey, K. R. A. Hazzard, A. M. Rey, D. S. Jin, and J. Ye, Observation of dipolar spin-exchange interactions with lattice-confined polar molecules, *Nature (London)* **501**, 521 (2013).
- [23] A. Patscheider, B. Zhu, L. Chomaz, D. Petter, S. Baier, A.-M. Rey, F. Ferlaino, and M. J. Mark, Controlling dipolar exchange interactions in a dense three-dimensional array of large-spin fermions, *Phys. Rev. Res.* **2**, 023050 (2020).
- [24] L. Christakis, J. S. Rosenberg, R. Raj, S. Chi, A. Morningstar, D. A. Huse, Z. Z. Yan, and W. S. Bakr, Probing site-resolved correlations in a spin system of ultracold molecules, *Nature (London)* **614**, 64 (2023).
- [25] A. Micheli, G. K. Brennen, and P. Zoller, A toolbox for lattice-spin models with polar molecules, *Nat. Phys.* **2**, 341 (2006).
- [26] L. Chomaz, I. Ferrier-Barbut, F. Ferlaino, B. Laburthe-Tolra, B. L. Lev, and T. Pfau, Dipolar physics: A review of experiments with magnetic quantum gases, *Rep. Prog. Phys.* **86**, 026401 (2023).
- [27] G. M. Bruun and E. Taylor, Quantum phases of a two-dimensional dipolar Fermi gas, *Phys. Rev. Lett.* **101**, 245301 (2008).
- [28] N. R. Cooper and G. V. Shlyapnikov, Stable topological superfluid phase of ultracold polar fermionic molecules, *Phys. Rev. Lett.* **103**, 155302 (2009).
- [29] J. Quintanilla, S. T. Carr, and J. J. Betouras, Metanematic, smectic, and crystalline phases of dipolar fermions in an optical lattice, *Phys. Rev. A* **79**, 031601(R) (2009).
- [30] C. Lin, E. Zhao, and W. V. Liu, Liquid crystal phases of ultracold dipolar fermions on a lattice, *Phys. Rev. B* **81**, 045115 (2010).
- [31] K. Mielsonson and J. K. Freericks, Density-wave patterns for fermionic dipolar molecules on a square optical lattice: Mean-field-theory analysis, *Phys. Rev. A* **83**, 043609 (2011).
- [32] L. He and W. Hofstetter, Supersolid phase of cold fermionic polar molecules in two-dimensional optical lattices, *Phys. Rev. A* **83**, 053629 (2011).
- [33] A.-L. Gadsbølle and G. M. Bruun, Harmonically trapped dipolar fermions in a two-dimensional square lattice, *Phys. Rev. A* **85**, 021604(R) (2012).
- [34] A.-L. Gadsbølle and G. M. Bruun, Dipolar fermions in a two-dimensional lattice at nonzero temperature, *Phys. Rev. A* **86**, 033623 (2012).
- [35] S. G. Bhongale, L. Mathey, S.-W. Tsai, C. W. Clark, and E. Zhao, Bond order solid of two-dimensional dipolar fermions, *Phys. Rev. Lett.* **108**, 145301 (2012).
- [36] S. G. Bhongale, L. Mathey, S.-W. Tsai, C. W. Clark, and E. Zhao, Unconventional spin-density waves in dipolar Fermi gases, *Phys. Rev. A* **87**, 043604 (2013).
- [37] E. G. C. P. van Loon, M. I. Katsnelson, and M. Lemeshko, Ultralong-range order in the Fermi-Hubbard model with long-range interactions, *Phys. Rev. B* **92**, 081106(R) (2015).
- [38] E. G. C. P. van Loon, M. I. Katsnelson, L. Chomaz, and M. Lemeshko, Interaction-driven Lifshitz transition with dipolar fermions in optical lattices, *Phys. Rev. B* **93**, 195145 (2016).
- [39] L. Chomaz, D. Petter, P. Ilzhöfer, G. Natale, A. Trautmann, C. Politi, G. Durastante, R. M. W. van Bijnen, A. Patscheider, M. Sohmen, M. J. Mark, and F. Ferlaino, Long-lived and transient supersolid behaviors in dipolar quantum gases, *Phys. Rev. X* **9**, 021012 (2019).
- [40] F. Böttcher, J.-N. Schmidt, M. Wenzel, J. Hertkorn, M. Guo, T. Langen, and T. Pfau, Transient supersolid properties in an array of dipolar quantum droplets, *Phys. Rev. X* **9**, 011051 (2019).
- [41] L. Tanzi, E. Lucioni, F. Famà, J. Catani, A. Fioretti, C. Gabbanini, R. N. Bisset, L. Santos, and G. Modugno, Observation of a dipolar quantum gas with metastable supersolid properties, *Phys. Rev. Lett.* **122**, 130405 (2019).
- [42] C. Lagoin, U. Bhattacharya, T. Grass, R. W. Chhajlany, T. Salamon, K. Baldwin, L. Pfeiffer, M. Lewenstein, M. Holzmann, and F. Dubin, Extended Bose-Hubbard model with dipolar excitons, *Nature (London)* **609**, 485 (2022).
- [43] Q. Li, B. Cheng, M. Chen, B. Xie, Y. Xie, P. Wang, F. Chen, Z. Liu, K. Watanabe, T. Taniguchi, S.-J. Liang, D. Wang, C. Wang, Q.-H. Wang, J. Liu, and F. Miao, Tunable quantum criticalities in an isospin extended Hubbard model simulator, *Nature (London)* **609**, 479 (2022).
- [44] T. Hensgens, T. Fujita, L. Janssen, X. Li, C. J. Van Diepen, C. Reichl, W. Wegscheider, S. Das Sarma, and L. M. K. Vandersypen, Quantum simulation of a Fermi-Hubbard model using a semiconductor quantum dot array, *Nature (London)* **548**, 70 (2017).
- [45] X. Wang, E. Khatami, F. Fei, J. Wyrick, P. Namboodiri, R. Kashid, A. F. Rigosi, G. Bryant, and R. Silver, Experimental realization of an extended Fermi-Hubbard model using a 2D lattice of dopant-based quantum dots, *Nat. Commun.* **13**, 6824 (2022).
- [46] S. Baier, M. J. Mark, D. Petter, K. Aikawa, L. Chomaz, Z. Cai, M. Baranov, P. Zoller, and F. Ferlaino, Extended Bose-Hubbard models with ultracold magnetic atoms, *Science* **352**, 201 (2016).
- [47] K. Góral and L. Santos, Ground state and elementary excitations of single and binary Bose-Einstein condensates of trapped dipolar gases, *Phys. Rev. A* **66**, 023613 (2002).
- [48] H. H. Roomany, H. W. Wyld, and L. E. Holloway, New method for the Hamiltonian formulation for lattice spin systems, *Phys. Rev. D* **21**, 1557 (1980).
- [49] E. R. Gagliano, E. Dagotto, A. Moreo, and F. C. Alcaraz, Correlation functions of the antiferromagnetic Heisenberg model using a modified Lanczos method, *Phys. Rev. B* **34**, 1677 (1986).
- [50] H.-Q. Lin, J. E. Gubernatis, H. Gould, and J. Tobochnik, Exact diagonalization methods for quantum systems, *Comput. Phys.* **7**, 400 (1993).
- [51] P. G. J. van Dongen, Extended Hubbard model at strong coupling, *Phys. Rev. B* **49**, 7904 (1994).
- [52] V. J. Emery, Theory of the quasi-one-dimensional electron gas with strong “onsite” interactions, *Phys. Rev. B* **14**, 2989 (1976).
- [53] D. J. Earl and M. W. Deem, Parallel tempering: Theory, applications, and new perspectives, *Phys. Chem. Chem. Phys.* **7**, 3910 (2005).
- [54] L. W. Cheuk, M. A. Nichols, M. Okan, T. Gersdorf, V. V. Ramasesh, W. S. Bakr, T. Lompe, and M. W. Zwierlein, Quantum-gas microscope for fermionic atoms, *Phys. Rev. Lett.* **114**, 193001 (2015).
- [55] M. F. Parsons, A. Mazurenko, C. S. Chiu, G. Ji, D. Greif, and M. Greiner, Site-resolved measurement of the spin-correlation function in the Fermi-Hubbard model, *Science* **353**, 1253 (2016).
- [56] M. Boll, T. A. Hilker, G. Salomon, A. Omran, J. Nespolo, L. Pollet, I. Bloch, and C. Gross, Spin- and density-resolved

- microscopy of antiferromagnetic correlations in Fermi-Hubbard chains, *Science* **353**, 1257 (2016).
- [57] L. W. Cheuk, M. A. Nichols, K. R. Lawrence, M. Okan, H. Zhang, E. Khatami, N. Trivedi, T. Paiva, M. Rigol, and M. W. Zwierlein, Observation of spatial charge and spin correlations in the 2D Fermi-Hubbard model, *Science* **353**, 1260 (2016).
- [58] E. Dagotto, J. Riera, Y. C. Chen, A. Moreo, A. Nazarenko, F. Alcaraz, and F. Ortolani, Superconductivity near phase separation in models of correlated electrons, *Phys. Rev. B* **49**, 3548 (1994).
- [59] W.-M. Huang, C.-Y. Lai, C. Shi, and S.-W. Tsai, Unconventional superconducting phases for the two-dimensional extended Hubbard model on a square lattice, *Phys. Rev. B* **88**, 054504 (2013).
- [60] W.-C. Chen, Y. Wang, and C.-C. Chen, Superconducting phases of the square-lattice extended Hubbard model, *Phys. Rev. B* **108**, 064514 (2023).
- [61] M. Yao, D. Wang, and Q.-H. Wang, Determinant quantum Monte Carlo for the half-filled Hubbard model with nonlocal density-density interactions, *Phys. Rev. B* **106**, 195121 (2022).
- [62] S. D. A. Sousa-Júnior, N. C. Costa, and R. R. dos Santos, Phase diagram for the extended Hubbard model on a square lattice, [arXiv:2304.08683](https://arxiv.org/abs/2304.08683).
- [63] A. W. Sandvik, Multichain mean-field theory of quasi-one-dimensional quantum spin systems, *Phys. Rev. Lett.* **83**, 3069 (1999).
- [64] I. Affeck, M. P. Gelfand, and R. R. P. Singh, A plane of weakly coupled Heisenberg chains: Theoretical arguments and numerical calculations, *J. Phys. A* **27**, 7313 (1994).
- [65] K. Hukushima and K. Nemoto, Exchange Monte Carlo method and application to spin glass simulations, *J. Phys. Soc. Jpn.* **65**, 1604 (1996).
- [66] W. Wang, J. Machta, and H. G. Katzgraber, Comparing Monte Carlo methods for finding ground states of Ising spin glasses: Population annealing, simulated annealing, and parallel tempering, *Phys. Rev. E* **92**, 013303 (2015).
- [67] D. J. Earl and M. W. Deem, Optimal allocation of replicas to processors in parallel tempering simulations, *J. Phys. Chem. B* **108**, 6844 (2004).
- [68] A. Kone and D. A. Kofke, Selection of temperature intervals for parallel-tempering simulations, *J. Chem. Phys.* **122**, 206101 (2005).